Inorganic Chemistry

pubs.acs.org/IC Article

Ternary Zinc Antimonides Unlocked Using Hydride Synthesis

Volodymyr Gvozdetskyi, Shannon J. Lee, Bryan Owens-Baird, Juli-Anna Dolyniuk, Tori Cox, Renhai Wang, Zijing Lin, Kai-Ming Ho, and Julia V. Zaikina*

Cite This: *Inorg. Chem.* 2021, 60, 10686−10697 Read Online

ACCESS | Metrics & More | Article Recommendations | Supporting Information

ABSTRACT: Three new sodium zinc antimonides $Na_{11}Zn_2Sb_5$, $Na_4Zn_9Sb_9$, and $NaZn_3Sb_3$ were synthesized utilizing sodium hydride NaH as a reactive sodium source. In comparison to the synthesis using sodium metal, salt-like NaH can be ball-milled, leading to the easy and uniform mixing of precursors in the desired stoichiometric ratios. Such comprehensive compositional control enables a fast screening of the Na−Zn−Sb system and identification of new compounds, followed by their preparation in bulk with high purity. $Na_{11}Zn_2Sb_5$ crystallizes in the triclinic $P\bar{1}$ space group (*No.* 2, $Z = 2$, $a = 8.8739(6)$ Å, $b = 10.6407(7)$ Å, $c = 11.4282(8)$ Å, $\alpha = 103.453(2)°$, $\beta = 96.997(2)°$, $\gamma = 107.517(2)°$) and features polyanionic $[Zn_2Sb_5]^{11-}$ clusters with unusual 3-coordinated Zn atoms. Both $Na_4Zn_9Sb_9$ ($Z = 4$, $a = 28.4794(4)$ Å, $b = 4.47189(5)$ Å, $c = 17.2704(2)$ Å, $\beta = 98.3363(6)°$) and $NaZn_3Sb_3$ ($Z = 8$, $a = 32.1790(1)$ Å, $b = 4.51549(1)$ Å, $c = 9.64569(2)$ Å, $\beta = 98.4618(1)°$) crystallize in the monoclinic $C2/m$ space group (*No.* 12) and have complex new structure types. For both compounds, their frameworks are built from $ZnSb_4$ distorted tetrahedra, which are linked via edge-, vertex-sharing, or both, while Na cations fill in the framework channels. Due to the complex structures, $Na_4Zn_9Sb_9$ and $NaZn_3Sb_3$ compounds exhibit low thermal conductivities (0.97−1.26 $W \cdot m^{-1}$ K^{-1}) at room temperature, positive Seebeck coefficients (19−32 μV/K) suggestive of holes as charge carriers, and semimetallic electrical resistivities ($\sim 1.0-2.3 \times 10^{-4}$ $\Omega \cdot m$). $Na_4Zn_9Sb_9$ and $NaZn_3Sb_3$ decompose into the equiatomic NaZnSb above ~800 K, as determined by *in situ* synchrotron powder X-ray diffraction. The discovery of multiple ternary compounds highlights the importance of judicious choice of the synthetic method.

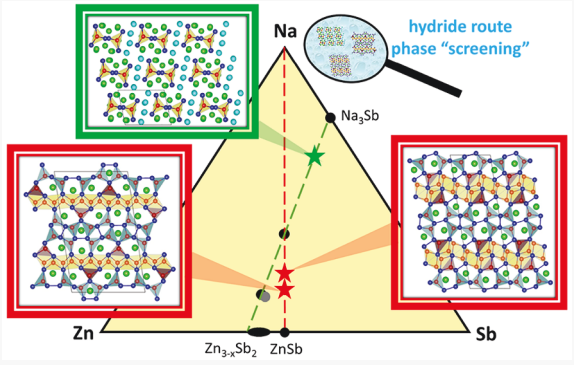

INTRODUCTION

Materials discovery requires the vigilant selection of a number of synthetic parameters (i.e., composition, precursors, temperature, pressure) for a successful outcome. Traditional solid-state synthesis operates at elevated temperatures and requires extended annealing times due to the slow diffusion between solid precursors. Moreover, it is often limited to the scarce number of thermodynamically stable phases. In contrast, a recently developed hydride synthetic route[1−18] is considerably faster, aided by the salt-like nature of metal hydrides, which allows for a thorough mixing of precursors and the elemental homogeneity of the starting mixture; this leads to a lower synthetic temperature and provids access to hindered metastable phases.

Ternary systems that have benefited from the implementation of the metal hydride synthesis route are the alkali metal−zinc−antimony systems. These systems have only briefly been explored previously. The ductility of alkali metals and high vapor pressures of Zn at elevated temperatures are significant synthetic hurdles that can result in side reactions and inhomogeneous products. Only 12 ternary compounds from *A*−Zn−Sb (*A* = alkali metal) systems can be found in the Inorganic Crystal Structure Database (ICSD)[19] and literature: LiZnSb, Li_2ZnSb, NaZnSb, $NaZn_4Sb_3$, *HT*-$Na_{1-y}Zn_{4-y}Sb_3$, KZnSb, $K_{8-x}Zn_{18+3x}Sb_{16}$, $K_{58}Zn_{122}Sb_{207}$, $Cs_8Zn_{18}Sb_{28}$, CsZnSb, RbZnSb, and $Rb_2Zn_5Sb_4$.[10,14−16,20−26] Among these, $Cs_8Zn_{18}Sb_{28}$ is the first antimony-based clathrate I,[26] $K_{58}Zn_{122}Sb_{207}$ represents novel clathrate XI,[16] and LiZnSb was theoretically predicted to show remarkable thermoelectric performance, *e.g.*, ability to convert heat into electricity and *vice versa*.[21] Remarkably, inexpensive and nontoxic binaries (Zn_4Sb_3, $Zn_{13}Sb_{10}$, Zn_8Sb_7, Zn_3Sb_2, ZnSb)[27−32] and ternary zinc (or cadmium) antimonides (family of $Ae(Zn/Cd)_2Sb_2$ compounds (*Ae* = Ca, Sr, Ba, Eu, or Yb),[33−37] Eu_2ZnSb_2,[38] and $Ca_{9-y}Eu_yZn_{4+x}Sb_9$[39]) as well as other related Zintl phases[40] attract attention for their thermoelectric properties.[41,42] For that reason, a comprehensive investigation of the unexplored *A*−Zn-Sb systems is highly desirable.

Hydride synthetic route allows for fast compositional "screening" and rapid discovery of new phases, oftentimes not accessible by traditional methods. As we recently showed,

Received: May 6, 2021
Published: June 28, 2021

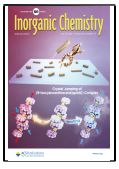

https://doi.org/10.1021/acs.inorgchem.1c01381
Inorg. Chem. 2021, 60, 10686−10697

ternary compounds in the Na−Zn−Sb ($NaZn_4Sb_3$) and K−Zn−Sb ($K_{8-x}Zn_{18+3x}Sb_{16}$ and the novel clathrate-XI $K_{58}Zn_{122}Sb_{207}$) systems can rapidly be prepared (<1 day) with high purity by the hydride route, starting from NaH or KH as precursors.[10,15,16] Despite the advantages of the hydride route, it yields only "final products" of the reaction, *e.g.*, phases that are stable at a particular temperature and pressure. *In situ* high-temperature powder X-ray or neutron diffraction can shed light on complex equilibria in multicomponent systems and hint at new metastable phases,[43−46] allowing the "screening" of temperature ranges of stability for new phases more effectively. Indeed, investigations of the thermal stability of NaZnSb and $NaZn_4Sb_3$ phases not only resulted in the discovery of a *HT*-$Na_{1-x}Zn_{4-x}Sb_3$ compound[14,15] but also hinted at the existence of other ternary phases in the Na−Zn−Sb system. Guided by *in situ* powder X-ray diffraction data, we continued the exploration of this system and localized three new ternary compounds. In this article, we report on the crystal and electronic structures, thermal stability determined by *in situ* X-ray diffraction, and thermoelectric properties for three new compounds: $Na_{11}Zn_2Sb_5$ ($K_{11}Cd_2Sb_5$ structure type), $Na_4Zn_9Sb_9$, and $NaZn_3Sb_3$ (both featuring new structure types).

EXPERIMENTAL SECTION

Synthesis. Starting materials for synthesis were used as received: sodium hydride (NaH, Sigma-Aldrich, 95%), sodium metal (Na, Alfa Aesar, 99.95%), zinc powder (Zn, Alfa Aesar, 99.996%), and antimony lump (Sb, Alfa Aesar, 99.9999%). All manipulations of reagents and samples were carried out under an inert argon atmosphere ($p(O_2)$ < 1 ppm, $p(H_2O)$ < 1 ppm) in a glovebox (LC-Technology).

Hydride Route. Antimony powders were prepared by ball-milling of antimony lumps for 12 min in ambient atmosphere using a standard grinding set with tungsten carbide inserts and high-energy ball-mill SPEX 8000 M MIXER/MILL. Afterward, in the argon-filled glovebox, powders of the sodium hydride, zinc, and pulverized antimony were weighed in 12:2:5.3, 4.5:9:9, and 1.1:3:3.3 molar ratio (total weight = 0.3 g) and loaded into a polycarbonate grinding set with a methacrylate grinding ball. The vials were further sealed into two plastic bags under argon atmosphere and removed from the glovebox for ball-milling. Samples were ball-milled for 12 min to achieve sufficient mixing, while longer ball-milling caused partial decomposition of NaH. Inside the glovebox, freshly prepared fine powders were loaded into tantalum containers, which were further arc-welded shut. The sealed tantalum ampules were placed into silica reactors equipped with Swagelok safety check valve to prevent overpressurizing of the reactors due to hydrogen gas release during the heat treatment. The silica reactors were evacuated to 4×10^{-5} bar and placed into a resistance furnace (Thermo Scientific Thermolyne Type FD1500M) equipped with a temperature controller (Eurotherm 3216). For the preparation of $NaZn_3Sb_3$ and $Na_{11}Zn_2Sb_5$, samples were slowly (1.4 K/min) heated from room temperature to 723 K, held at that temperature for 8 h, and cooled to room temperature naturally by switching off the furnace. In the case of $Na_4Zn_9Sb_9$, samples were heated (1.4 K/min) to 773 K, held there for 8 h, and quenched into cold water. $Na_{11}Zn_2Sb_5$ is extremely air- and moisture-sensitive, while the other two phases are stable in air.

Growth of Single Crystals from Elements. To obtain crystals suitable for single crystal X-ray diffraction, synthesis from elements and a heating profile with a slow cooling step were employed. For single crystal growth of $Na_4Zn_9Sb_9$ and $NaZn_3Sb_3$, elemental Na, Zn, and Sb (molar ratio of Na:Zn:Sb = 4.5:9:9, 1.1:3:3.3) were loaded into carbon-coated silica tubes, which were flame-sealed under a vacuum and heated from room temperature to 873 K (2 K/min), held at that temperature for 24 h, slowly cooled to 473 K at a rate of 0.04 K/min, and then allowed to cool naturally to room temperature by switching off the furnace. Samples were found to be inhomogeneous and comprised of a mixture of powders and chunks with different colors/shapes. Single crystals of the $Na_4Zn_9Sb_9$ and $NaZn_3Sb_3$ compounds were mechanically separated from the powders of NaZnSb. Additionally, traces of ZnSb, $NaZn_4Sb_3$, and Sb were present as impurities within the samples. For single crystal growth of the $Na_{11}Zn_2Sb_5$ compound, elemental Na, Zn, and Sb (molar ratio of Na:Zn:Sb = 12:2:5.3) were loaded in a tantalum tube, which was further sealed in an argon atmosphere and heated to 773 K (1.6 K/min), held at that temperature for 8 h, slowly cooled to 523 K at a rate of 0.015 K/min, and then allowed to naturally cool to room temperature by switching off the furnace. Single crystals of the target phase were mechanically separated from the powders of NaZnSb and Na_3Sb.

Characterization. *Laboratory Powder X-ray Diffraction (PXRD).* The purity of polycrystalline samples was checked by means of a Rigaku MiniFlex600 powder diffractometer with Cu Kα radiation (λ = 1.540593 Å) and Ni Kβ filter. Data were collected on a zero-background plate holder in air at room temperature. In case of $Na_{11}Zn_2Sb_5$, powders were loaded in a holder designed for air-sensitive powders. Phase analysis was performed using the PDF-2 database incorporated into PDXL program software.[47]

Single-Crystal X-ray Diffraction (SC-XRD). Single crystal data were collected by means of a Bruker D8 VENTURE diffractometer (Photon CMOS detector, Mo−IμS microsource and Oxford Cryosystem 800 low temperature device) at 100 K. Data integration, absorption correction, and unit cell determination was performed by the APEX 3 software.[48] The starting atomic parameters were obtained by direct methods with the SHELXS-2017.[49] Subsequently, the structures were refined using SHELXL-2017[49] (full-matrix least-squares on F_o^2).

More than two dozen of the $Na_4Zn_9Sb_9$ and $NaZn_3Sb_3$ crystals were tested and found to be extensively twinned and weakly diffracting. Even after the isolation and separation of twinned domains, the results of crystal structure refinements did not considerably improve due to the inherent crystals imperfection. Therefore, we used a combination of SC XRD (crystal solution) with high-resolution synchrotron PXRD (structure refinement) to elucidate the crystal structures of $Na_4Zn_9Sb_9$ and $NaZn_3Sb_3$. As shown below, the refinement of the models determined from the single crystal XRD using high resolution synchrotron PXRD resulted in low *R*-factors R_B = 0.11 ($Na_4Zn_9Sb_9$) and R_B = 0.09 ($NaZn_3Sb_3$), proving that these models correctly represent the materials in bulk.

Only basic crystallographic parameters, i.e., syngony, cell dimensions, and tentative structural models, though with reasonable interatomic distances, were extracted from the $Na_4Zn_9Sb_9$ single crystal X-ray diffraction data sets (Tables S1−S4). Analysis of the diffraction data of $Na_4Zn_9Sb_9$ revealed monoclinic symmetry (a = 28.354(3) Å, b = 4.4614(5) Å, c = 17.218(2) Å, β = 98.313(2)°), centrosymmetric space group $C2/m$. Sb atoms were found to occupy nine 4*i* sites, Zn−nine 4*i* sites, and Na−four 4*i* sites (Table S2). Despite the modest quality of single crystals, analysis of the intensity of the first 20 residual electron density peaks on the difference Fourier map from three single crystal data sets clearly indicates the two electron density peaks (Figure S1) located near the Zn(8) site (at distance of ∼1.84 and 1.21 Å). Therefore, a split-model was introduced: two additional atomic sites Zn(10) in 4*i* and Zn(11) in 4*i* in the close proximity to Zn(8). Independent refinement of the Zn(8), Zn(10), and Zn(11) site occupancy factors (*s.o.f.*) resulted in 0.75(2), 0.23(2), 0.18(2) (SC1), and 0.81(3), 0.16(2), 0.13(2) (SC2) respectively. Analysis of the diffraction data from another single crystal (SC3) selected from the sample prepared from NaCl flux revealed the same structure (Table S4), while the *s.o.f.* for the split sites Zn(8), Zn(10), Zn(11) were refined to 0.77(1), 0.13(1), 0.12(1). Taking into account that (i) the Zn(10)−Zn(11) distance of ∼2.73 Å is typical for Zn-containing compounds,[19] (ii) independently refined *s.o.f.* for Zn(10) is the same as that for Zn(11) within two standard deviations, and (iii) the sum *s.o.f.*'s for Zn(8) and Zn(10) & Zn(11) was refined to unity, we suggest that either Zn(8) or the Zn(10)−Zn(11) pair is present in the structure. Therefore, during the last cycles of refinements, *s.o.f.* for Zn(10) and Zn(11) sites were

https://doi.org/10.1021/acs.inorgchem.1c01381
Inorg. Chem. 2021, 60, 10686−10697

constrained to be the same, while the sum of *s.o.f.*'s for Zn(8), Zn(10), and Zn(11) was constrained to unity and atomic displacement parameters (ADP) for Zn(8), Zn(10), Zn(11) were constrained to be the same. Such refinement led to the following *s.o.f.*s for Zn(8) and Zn(10)−Zn(11) pair: 0.78(1)/0.22(1), 0.85(1)/0.15(1) and 0.874(8)/0.126(8) for each SC-XRD data set, respectively (Tables S2−S4). Considering the small deviation from 4:9:9 composition, the compound is referred to as $Na_4Zn_9Sb_9$ for simplicity further in the text.

Twinning, Crystal Imperfection, and Disorder Problem. We have attempted to separate twinned domains while analyzing the SC3 data set, but the results of crystal structure refinement (Table S1) showed only slightly reduced $R_1 = 0.075$ and $wR_2 = 0.122$ compared to those of the "raw" data set ($R_1 = 0.078$ and $wR_2 = 0.180$). In addition, another data set (SC2) showed an exceptional coherence with the monoclinic unit cell as evidenced from the X-ray diffraction images (Figure S2). However, the structure refinement using SC2 data set still resulted in relatively high $R_1 = 0.067$ and $wR_2 = 0.171$ and residual electron density present (Table S1). Since merohedral twinning does not occur in the monoclinic system, and there is no indication of non-merohedral twining for SC2 data set, we believe that crystals' inherent imperfections and local disorder might be the main reasons for high *R* factors. Refinement in the lower symmetry (triclinic *P*1 space group) did not result in the lower *R*-factor. Moreover, analysis of the atomic coordinates (*P*1) using the program PLATON (command ADDSYM)[50] indicated that the actual symmetry is *C*2/*m*.

Due to the weak intensity of reflections and insufficient crystal quality of $NaZn_3Sb_3$, the tentative structure solution was obtained first in triclinic syngony (space group $P\bar{1}$, $Z = 8$, $a = 8.948(7)$ Å, $b = 9.553(7)$ Å, $c = 16.07(1)$ Å, $\alpha = 98.42(1)°$, $\beta = 97.99(1)°$, $\gamma = 97.06(1)°$). The further symmetry analysis of the atomic coordinates using the program PLATON (command ADDSYM)[50] indicated that the actual symmetry of the structure is monoclinic, space group *C*2/*m*, $Z = 8$, $a = 31.83(2)$ Å, $b = 4.473(3)$ Å, $c = 9.551(7)$ Å, $\beta = 98.51(2)°$. Sb atoms were found to occupy six 4*i* sites, Zn−six 4*i* sites, and Na−two 4*i* sites (Tables S5, S6). The preliminary structural models of $Na_4Zn_9Sb_9$ and $NaZn_3Sb_3$ were further refined using high-resolution synchrotron powder X-ray diffraction data (*vide infra*).

Crystals of $Na_{11}Zn_2Sb_5$ were considerably larger and stronger diffracting. Analysis of the diffraction data revealed triclinic symmetry, centrosymmetric space group $P\bar{1}$, $a = 8.8739(6)$ Å, $b = 10.6407(7)$ Å, $c = 11.4282(8)$ Å, $\alpha = 103.453(2)°$, $\beta = 96.997(2)°$, $\gamma = 107.517(2)°$. Sb atoms were found to occupy five 2*i* sites, Zn−two 2*i* sites, and Na−eleven 2*i* sites. Details of the data collection and refinement are summarized in Table S7; atomic coordinates and ADPs are given in Table S8.

Synchrotron Powder X-ray Diffraction. High-resolution synchrotron powder diffraction data were collected at beamline 11-BM at the Advanced Photon Source (APS), Argonne National Laboratory (ANL) with a wavelength $\lambda = 0.412682$ Å. Data for $Na_4Zn_9Sb_9$ and $NaZn_3Sb_3$ compounds loaded into Kapton capillaries were collected at room temperature and ambient pressure. Diffraction patterns were analyzed by Rietveld refinement method using the GSAS-II software package.[51] The profile parameters, background parameters, zero correction, and cell parameters were refined first. The background was fitted using 24-point linear interpolation. A pseudo-Voigt function was applied to generate the profile shape. The preferential orientation of crystallites was taken into account. Refinement of the models determined from the single crystal X-ray diffraction results in low factors $R_B = 11\%$ ($Na_4Zn_9Sb_9$) and $R_B = 9\%$ ($NaZn_3Sb_3$) (Tables S9−S11, Figure S5, S6). The powder X-ray diffraction was not sensitive to confirm the split positions Zn(8), Zn(10), Zn(11) found in the structure of $Na_4Zn_9Sb_9$ from single crystal data.

High-temperature synchrotron powder X-ray diffraction data (HT-PXRD) was collected at beamline 17-BM (APS ANL) with wavelengths $\lambda = 0.24130$ Å ($NaZn_3Sb_3$) and $\lambda = 0.24141$ Å ($Na_4Zn_9Sb_9$). Powdered samples were filled in 0.7 mm outer diameter thick-wall (0.1 mm) silica capillaries, which were flame-sealed under a vacuum. The capillaries were mounted into a secondary shield capillaries (0.9 mm inner diameter, 1.1. mm outer diameter) located on a sample stage equipped with two resistive microheaters and a thermocouple. Further details of this experimental setup can be found elsewhere.[52] Data was collected upon heating and cooling in the temperature range 298 K → 900 K → 298 K with variable heating and cooling rate ∼10−20 K·min^{-1}.

Spark-Plasma Sintering. Bulk samples of $Na_4Zn_9Sb_9$ and $NaZn_3Sb_3$ prepared via the hydride route were consolidated into dense pellets using Spark Plasma Sintering (SPS). In an argon-filled glovebox, the powdered samples were loaded into a small graphite die (inner diameter 5 mm) between several circles of graphite foil and enclosed with tungsten carbide plungers. The smaller die was assembled, inserted into a larger outer graphite die with graphite plungers (inner diameter 20 mm) and transported to the SPS Dr. Sinter Lab Jr. SPS-211Lx (Sumitomo Coal Mining Co., Ltd.) keeping the assembly under an inert atmosphere. The sample of $NaZn_3Sb_3$ was sintered by slow heating to 448 K over a period of 8 min under a uniaxial pressure of 115 MPa and dwelling for 2 min. The sintering uniaxial pressure was lowered to 21 MPa in the case of $Na_4Zn_9Sb_9$, and the same temperature profile was used. The use of higher pressure led to the compound's degradation. Afterward, the pressure was released, and sintered pellets were allowed to cool to room temperature. The pellets were removed from the graphite dies and polished to remove traces of the graphite foil. The geometrical densities of the pellets were ∼89% and 79% for $NaZn_3Sb_3$ and $Na_4Zn_9Sb_9$ phases, respectively, as compared to the calculated X-ray crystal densities. Elemental Sb was detected as the main impurity in sintered pellets (6 and 15 wt %, respectively).

Elemental Analysis. Elemental analysis was performed using FEI Quanta-250 field emission scanning electron microscope (SEM) equipped with an Oxford X-Max 80 detector and an Oxford Aztec energy-dispersive X-ray analysis system. Inside a glovebox, small chunks of the pellets sintered by SPS were mounted onto an aluminum holder designed for air-sensitive samples using double-sided conductive carbon tape. Samples were oriented with a flat side perpendicular to the beam and analyzed using a 15 kV accelerating voltage and an accumulation time of 60 s.

Combustion analysis was also performed to obtain hydrogen content for the samples of $Na_4Zn_9Sb_9$, $NaZn_3Sb_3$, $Na_{11}Zn_2Sb_5$. Elemental analysis results (% C, % H, % N) were acquired using a PE 2100 Series II combustion analyzer (PerkinElmer Inc., Waltham, MA) with acetanilide as a calibration standard and the combustion and reduction temperatures of 1198 and 913 K. All standards and reagents were from PerkinElmer and/or Elementar America's Inc. The determined H content is <0.03%, which is within the precision and accuracy of the measurement, thus no significant amount of H is present in the samples.

Thermoelectric Properties Measurement. Transport properties of the pellets sintered by SPS were measured in the 10−300 K temperature range using the Physical Properties Measurement System Evercool II (PPMS, Quantum Design). The Seebeck thermopower and thermal conductivity were measured using the Thermal Transport Option (TTO) in a two-probe configuration. Electrical resistivity was measured in a more accurate four-probe geometry using 50 μm platinum wires attached with silver paste and the Alternating Current Transport (ACT) option.

Differential Scanning Calorimetry Analysis. To evaluate the thermal stability of the phases, a differential scanning calorimetry (DSC) measurement was performed using a Netzsch 404 F3 Pegasus Differential Scanning Calorimeter. Powdered samples of $NaZn_3Sb_3$ and $Na_4Zn_{9,}Sb_9$ ($m \sim 50$ mg) were sealed inside an evacuated silica ampule, heated to 873 K, and cooled to room temperature with a rate of 10 K/min rate.

Computational Details. First-principles calculations were carried out based on density functional theory (DFT) using the VASP code.[53,54] The projected augmented-wave (PAW) method[55] was used to describe the electron−ion interaction, and the generalized gradient approximation (GGA) in the Predew-Burke-Ernzerhof (PBE) form[56,57] was employed for the exchange-correlation energy functional. A plane-wave basis with a kinetic energy cutoff of 650 eV was

https://doi.org/10.1021/acs.inorgchem.1c01381
Inorg. Chem. 2021, 60, 10686−10697

used. All atoms in the calculation cell were allowed to relax until the forces on each atom were smaller than 0.01 eV/Å. The projector augmented-wave method was used to describe the valence configuration: $3s^1$ for Na, $3d^{10}4s^2$ for Zn, and $5s^25p^3$ for Sb.

RESULTS AND DISCUSSION

Synthesis. Previously, it was shown that the hydride route is advantageous for the synthesis of different complex antimonides, arsenides, borides, germanides, and silicides.[1−18] Unlike ductile alkali and alkaline-earth metals, a salt-like nature of their hydrides allows for the implementation of a ball-milling technique in synthesis. Due to the thorough mixing of precursors in the hydride route, the sample compositions can be precisely controlled, yielding high purity materials. Another advantage of finely mixed reactants in the stoichiometric ratios is faster heat treatment at lower temperatures required for the complete reaction, as compared to the traditional solid-state synthesis. As it will be shown further, synthesis of all three new phases ($Na_4Zn_9Sb_9$, $NaZn_3Sb_3$, and $Na_{11}Zn_2Sb_5$) requires only 8 h of heat treatment at moderate temperatures (700−800 K) as opposed to several days for traditional solid state synthesis.

Analysis of PXRD patterns suggests that the samples synthesized using Na metal contain a considerable amount of impurities in addition to the target $Na_4Zn_9Sb_9$, $NaZn_3Sb_3$, and $Na_{11}Zn_2Sb_5$ compounds (Figures S7−S10), unlike samples prepared by the hydride (NaH) route. This is expected, considering the low degree of initial mixing and thus compositional inhomogeneity for the samples synthesized using Na metal. For example, $Na_4Zn_9Sb_9$ and $NaZn_3Sb_3$ compounds are compositionally similar to each other and to the NaZnSb and $NaZn_4Sb_3$ phases (Figure 1). We can achieve an intimate mixing of reactants by using NaH as a sodium source and target a specific compound by fine adjustments of the Na concentration. Unlike the stoichiometric molar ratio used for synthesis of ternary $NaZn_4Sb_3$ (NaH:Zn:Sb = 1:4:3),[15] the compound that was discovered earlier in this system, synthesis of $Na_{11}Zn_2Sb_5$, $Na_4Zn_9Sb_9$, and $NaZn_3Sb_3$ compounds required an optimization of nominal composition and temperature profiles used for the heat treatment. In the case of $NaZn_3Sb_3$, the stoichiometric molar ratio (NaH:Zn:Sb = 1:3:3) used for hydride route yields a considerable amount of $NaZn_4Sb_3$ impurity (Figure S8), together with traces of the binary ZnSb. Compositions richer in Na and Sb, i.e., NaH:Zn:Sb = 1.2:3:3.6 lead to the increased content of elemental Sb impurity and formation of $Na_4Zn_9Sb_9$ as a side product. The starting molar ratio of NaH:Zn:Sb = 1.1:3:3.3 was found to be optimal for the preparation of phase pure $NaZn_3Sb_3$. For $Na_4Zn_9Sb_9$, a composition of NaH:Zn:Sb = 4.5:9:9 and high temperature quenching of samples into cold water from 773 K was found to give the highest yield (89 wt %) of the target phase (Figure S9). NaH:Zn:Sb = 12:2:5.3 was determined to be the optimal loading ratio for $Na_{11}Zn_2Sb_5$ compound (Figure S10). Alternative routes for preparation of $Na_4Zn_9Sb_9$ using NaCl halide flux, binary NaSb precursor, elimination of Na from ternary NaZnSb under various conditions (see Supporting info) have been attempted, but never resulted in considerable yield of the target phase.

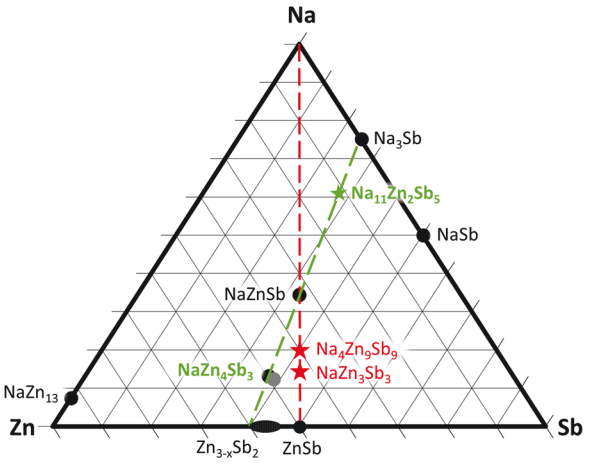

Figure 1. Compositional diagram for the ternary Na−Zn−Sb system. Na−ZnSb and Na_3Sb−$Zn_{3-x}Sb_2$ compositional lines are emphasized in red and green, respectively. A number of binary compounds in the vicinity of Zn:Sb = 3:2 composition have been previously reported ($Zn_{13}Sb_{10}$, Zn_8Sb_7, Zn_6Sb_5, Zn_4Sb_3, Zn_3Sb_2)[19,27−32] and are denoted as $Zn_{3-x}Sb_2$. The compositions of $NaZn_4Sb_3$ and structurally different *HT*-$Na_{1-x}Zn_{4-y}Sb_3$ phase are denoted as overlapping black/gray circles. The composition of new ternary phases reported here are shown with stars.

It is interesting to note that ternary compounds in the Na−Zn−Sb system (Figure 1) are found along two main compositional lines (red line: connecting Na and ZnSb; and green line: connecting Na_3Sb and $Zn_{3-x}Sb_2$) crossed at the composition of equiatomic phase NaZnSb. NaZnSb is the "final" phase that other ternaries (*e.g.*, $NaZn_4Sb_3$, *HT*-$Na_{1-x}Zn_{4-y}Sb_3$,[15] $Na_4Zn_9Sb_9$ and $NaZn_3Sb_3$; see below) are transformed/decomposed to upon heating. Considering the oxidation states for Na, Zn, and Sb as +1, + 2, and −3, respectively, thus assuming no Sb−Sb bonds present, compositions of electron balanced compounds are located on the green line (Figure 1): $(Zn^{2+})_3(Sb^{3-})_2$, $Na^+(Zn^{2+})_4(Sb^{3-})_3$, $Na^+Zn^{2+}Sb^{3-}$, $Na_{11}{}^+(Zn^{2+})_2(Sb^{3-})_5$, and $Na_3{}^+Sb^{3-}$. Compounds on the red line, ZnSb, $NaZn_3Sb_3$, and $Na_4Zn_9Sb_9$, are not electron balanced if standard oxidation states are used hinting at the presence of Sb−Sb bonds in these structures, as discussed below.

Crystal Structures. Structures of all three compounds have low symmetry and relatively large unit cells (~1000 Å^3). $Na_4Zn_9Sb_9$ (a = 28.4794(4) Å, b = 4.47189(5) Å, c = 17.2704(2) Å, β = 98.3363(6)°) and $NaZn_3Sb_3$ (a = 32.1790(1) Å, b = 4.51549(1) Å, c = 9.64569(2) Å, β = 98.4618(1)°) crystallize in the monoclinic $C2/m$ space group (Table S10, S11). Searches by Pearson symbol, unit cell metric, and Wyckoff sequences (i^{22}) and (i^{14}) in the Inorganic Crystal Structure database (ICSD)[19] indicate that $Na_4Zn_9Sb_9$ and $NaZn_3Sb_3$ crystallize in new structure types. Both structures (Figure 2 *a*, *b*) are built from Zn-centered Sb_4 distorted tetrahedra with Zn−Sb distances in the range of ~2.62−2.96 Å. These distances are typical for other ternary alkali metal zinc antimonides, *e.g.*, NaZnSb (2.76 Å),[14,23] $NaZn_4Sb_3$ (2.57−2.86 Å) and *HT*-$Na_{1-x}Zn_{4-y}Sb_3$ (2.57−2.94 Å),[15] $K_{8-x}Zn_{18+3x}Sb_{16}$ (2.63−2.95 Å),[10] *hex*-LiZnSb (2.67−2.76 Å),[20] $Rb_2Zn_5Sb_4$ (2.64−2.90 Å),[24] and binary zinc antimonide ZnSb (2.64−2.90 Å).[58] The Zn@Sb4 tetrahedra in structures of $Na_4Zn_9Sb_9$ and $NaZn_3Sb_3$ compounds are linked in three ways: via edge-sharing (*es*), via vertex-sharing (*vs*), or with the combination of both types. Edge-sharing (*es*) tetrahedra slabs are alternating with vertex-sharing (*vs*) tetrahedra blocks. Within the *vs*-tetrahedra blocks, there are channels hosting Na atoms (Figure 2a,b). Layers of *vs*-tetrahedra (Figure 2a,b, light blue) are present in both $NaZn_3Sb_3$ and $NaZn_9Sb_9$ and are linked to the layers of *es*-

https://doi.org/10.1021/acs.inorgchem.1c01381
Inorg. Chem. 2021, 60, 10686−10697

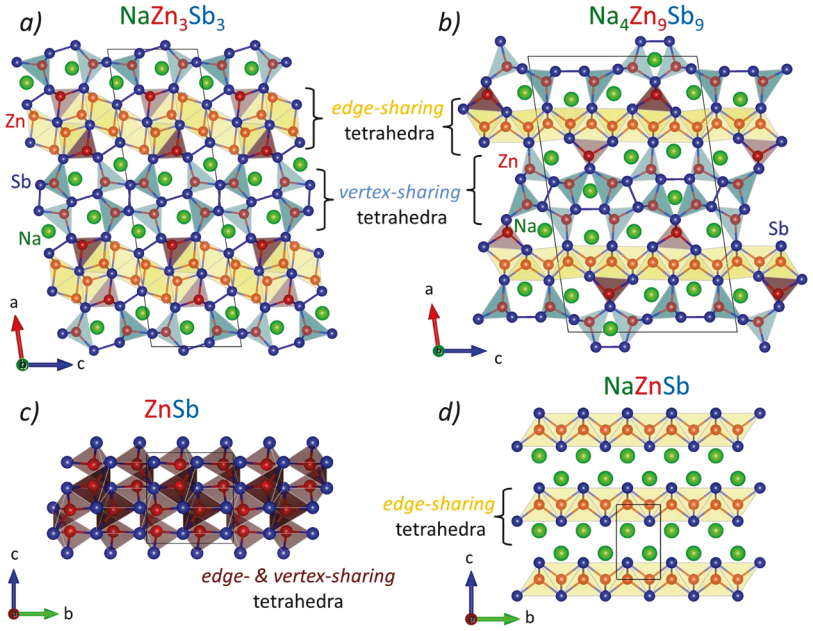

Figure 2. Crystal structures of (a) $NaZn_3Sb_3$ and (b) $Na_4Zn_9Sb_9$ in comparison with (c) ZnSb and (d) NaZnSb. Na, green; Zn, red; Sb, blue. In all cases, Zn is coordinated by four Sb forming distorted tetrahedra. Edge-sharing (*es*) tetrahedra (yellow) alternate with vertex-sharing (*vs*) tetrahedra (light blue) forming channels filled by Na cations. Bridging tetrahedra that feature edge- and vertex-sharing connectivity are shown in brown.

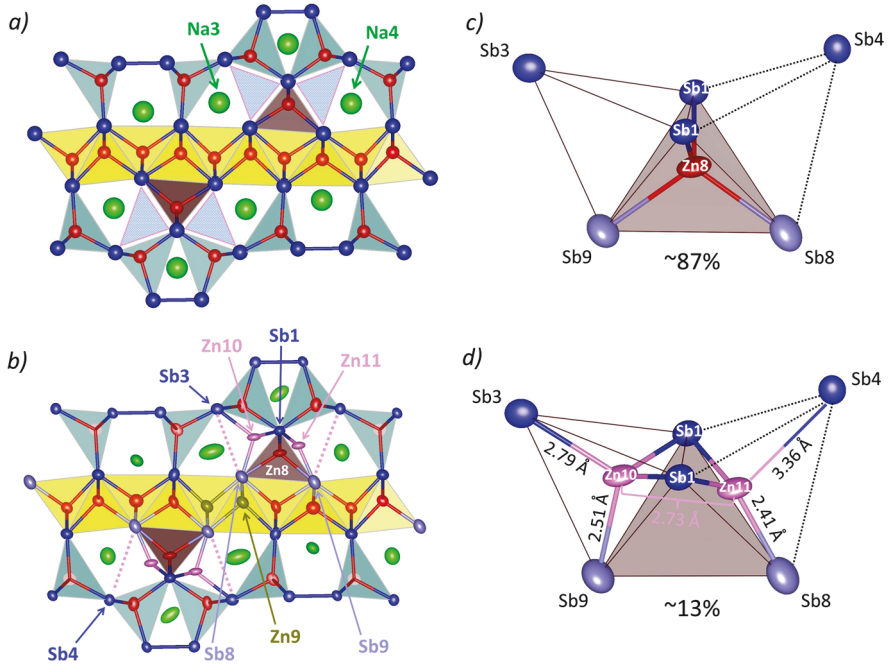

Figure 3. (a) Idealized crystal structure of $Na_4Zn_9Sb_9$ (gaps near Na(4) and Na(3) atoms are emphasized). (b) Crystal structure of $Na_4Zn_9Sb_9$ taking into account the split-sites model involving Zn(8), Zn(10), and Zn(11) atoms. (c) An isolated Zn(8)@Sb_4 tetrahedra, realized in ~87% of cases. (d) An isolated Zn(10)@Sb_4 and Zn(11)@Sb_4 tetrahedra, realized in ~13% of cases. This disorder causes enlargement of ADPs for adjacent Sb(9), Sb(8), and Zn(9) atoms, with displacement ellipsoids emphasized.

tetrahedra via another type of deformed tetrahedra (Figure 2a,b, brown). The latter shows both *vs*- and *es*-types of connectivity simultaneously, similar to the binary ZnSb (CdSb structure type, *Pbca*) (Figure 2 *c*). The planar layers of *es*-shared tetrahedra in the $Na_4Zn_9Sb_9$ structure are similar, albeit slightly deformed, to those found in the structure of the layered NaZnSb (PbClF, *P*4/*nmm*) (Figure 2d), while comparable layers of *es*-terahedra in the $NaZn_3Sb_3$ structure are considerably corrugated.

In the ideal structure of $Na_4Zn_9Sb_9$, Zn atoms are 4-coordinated by Sb. In turn, Sb atoms have diverse coordination numbers: Sb(1) is 4-coordinated by Zn; Sb(5), Sb(7), Sb(8), Sb(9) are 5-coordinated by Zn, while the rest of Sb atoms are 3-coordinated by Zn and additionally form pairs, *e.g.*, Sb(2)−Sb(6), Sb(3)−Sb(3), Sb(4)−Sb(4) with the interatomic distance of 2.8−2.9 Å, corresponding to covalent bond (Figure S3). For the purposes of electron counting, electropositive metals are considered as cations, *e.g.*, Na^+ and Zn^{2+}. To fulfill

https://doi.org/10.1021/acs.inorgchem.1c01381
Inorg. Chem. 2021, 60, 10686−10697

the octet rule, electronegative Sb is considered as an anion with either a −3 oxidation state (coordinated only to Zn atoms) or with a −2 oxidation state for those Sb atoms which are additionally coordinated to another Sb atom. Such electron count results in a nearly electron balanced composition with 1 electron deficiency per formula unit: $(Na^{+})_4(Zn^{2+})_9(Sb^{3-})_5(Sb^{2-})_4$ (Table S12).

In the $NaZn_3Sb_3$ structure, Sb(1) and Sb(6) atoms are coordinated by 5 Zn or 6 Zn atoms, respectively. In turn, each Sb(2), Sb(3), and Sb(5) are 3-coordinated by Zn atoms, and additionally by another Sb atom at a distance of 2.8−2.9 Å, thus homoatomic dumbbells Sb(2)−Sb(2), Sb(3)−Sb(4) and Sb(5)−Sb(5) form. Sb(4) is 4-coordinated by Zn atoms and additionally by one Sb atom (Figure S4). Similarly to the electron count for $Na_4Zn_9Sb_9$, Na and Zn are regarded as +1 and +2 cations, respectively. The −3 oxidation state is assigned to Sb atoms coordinated to Zn atoms only, while −2 oxidation state is assigned to Sb atoms engaged in covalently bonded Sb−Sb pairs. Such an assignment results in the electron balanced composition: $(Na^{+})_2(Zn^{2+})_6(Sb^{3-})_2(Sb^{2-})_4$.

A splitting of the Zn atomic sites (Zn(8), Zn(10), Zn(11)) is found in the structure of $Na_4Zn_9Sb_9$ determined from SC-XRD (Figure 3). In the ideal $Na_4Zn_9Sb_9$ structure (Figure 3*a*), there are two "empty" tetrahedral gaps (emphasized in Figure 3*a*) near the Na(3) and Na(4) atoms. If the split model is taken into account (Figure 3*b*), then ∼13% of the gaps are filled with Zn(10)−Zn(11) pairs (Zn−Zn interatomic distance is $d \sim 2.73$ Å). This disorder impacts the adjacent atoms causing a large atomic displacement parameter (ADP) for Sb(9) and Sb(8) atoms, as well as for the Zn(9) atom in the *es*-tetrahedra slab. (Figure 3b−d). The distance between the Zn(11) and Sb(4) atoms is considerably longer than the typical Zn−Sb distances in this structure (3.36 vs ∼2.80 Å). Disorder in Zn sites is common for binary Zn antimonides.[28,29,31,32]

Upon closer inspection, the coordination environments of all Na atoms in $NaZn_3Sb_3$ and $Na_4Zn_9Sb_9$ can be better described as polyhedra rather than channels, since their top and bottom pentagonal rings are significantly smaller than their central (also pentagonal) ring (Figure 4, Figures S11, S12). The Na(2)-centered polyhedra in $Na_4Zn_9Sb_9$ (pentagonal prism with 5 additional atoms) is the most recognizable and has been found in other polyhedral systems. In their 2011 review of tetrel clathrates, Pakkanen et al. [59] mentioned this 5^26^5 polyhedron (consisting of two pentagonal (5-member) and five hexagonal (6-member) faces, Figure 4, Na(2) environment) was an important structural element of intergrowth clathrates. The 5^26^5 cage is also a known structural unit of other ternary zinc antimonides, as in the case of $Eu_{11}Zn_6Sb_{12}$.[60] Nevertheless, the structures of $NaZn_3Sb_3$ and $Na_4Zn_9Sb_9$ compounds cannot be built exclusively from different types of Na-polyhedra, but as can be seen from Figures S11 and S12, additional $ZnSb_4$ tetrahedra as linking elements are required. Interestingly, in the $NaZn_3Sb_3$ structure, layers of Na-polyhedra are completely separated with layers of $ZnSb_4$ tetrahedra (Figure S12).

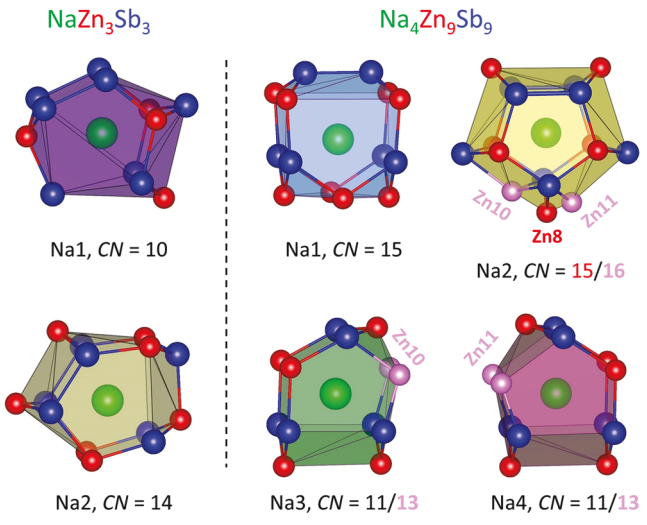

Figure 4. Different types of Na polyhedra in the structures of $NaZn_3Sb_3$ and $Na_4Zn_9Sb_9$.

Unlike other ternary compounds in the Na−Zn−Sb system, the crystal structure of $Na_{11}Zn_2Sb_5$ features polyanionic "butterfly-like" $[Zn_2Sb_5]^{11-}$ clusters with unusual tri-coordinated Zn atoms (Figure 5a). These $[Zn_2Sb_5]^{11-}$ anion clusters are embedded into Na^{+} nets similar to that in Na metal (W structure type) (Figure 5b). $Na_{11}Zn_2Sb_5$ is isostructural to the ternary antimonide $K_{11}Cd_2Sb_5$, the only other representative of this type.[61] Within the $[Zn_2Sb_5]^{11-}$ cluster (Figure 5d), Zn(1) and Zn(2) atoms are coordinated to two Sb atoms with bond distances of ∼2.65 Å, and additionally connected to a bridging Sb(4) atom, with a slightly longer bond distance of ∼2.74 Å. Similarly, longer distances to bridging Sb atoms were observed in the case of the $[Cd_2Sb_5]^{11-}$ cluster,[61] where two pairs of Cd−Sb distances (∼2.86 Å) are shorter compared to the two other Sb bridging bond distances (∼2.96 Å). Since no Sb−Sb contacts are formed, the simple assignment of oxidation states suggests that $Na_{11}Zn_2Sb_5$ is electron balanced: $(Na^{+})_{11}(Zn^{2+})_2(Sb^{3-})_5$.

Thermal Stability and Phase Transformation by *In Situ* HT-PXRD. High-temperature synchrotron powder X-ray diffraction (HT-PXRD) data for the samples of $Na_4Zn_9Sb_9$ and $NaZn_3Sb_3$ are shown in Figure 6. $Na_4Zn_9Sb_9$ starts to decompose at temperatures above 511 K into the more thermodynamically stable NaZnSb and elemental Sb. This process is finished above 791 K, when NaZnSb is the only crystalline phase present (excess of Zn and Sb is molten). The $NaZn_3Sb_3$ compound is stable upon heating up to 763 K and then abruptly decomposes into NaZnSb and *HT*-$Na_{1-x}Zn_{4-y}Sb_3$.[15] Above 812 K, only NaZnSb is observed. This makes the synthesis of $NaZn_3Sb_3$ and $Na_4Zn_9Sb_9$ compounds by conventional solid-state methods extremely challenging. From one point of view, high temperatures are needed to overcome a diffusion barrier between precursors. This will lead to the formation of the more stable NaZnSb, instead of the targets $NaZn_3Sb_3$ and $Na_4Zn_9Sb_9$. On the contrary, the hydride route, benefiting from high reactivity of hydrides and intimate mixing of the precursors by ball-milling, does not require high temperature, enabling the targeted preparation of $Na_4Zn_9Sb_9$ and $NaZn_3Sb_3$.

Differential scanning calorimetry (DSC) data for the $Na_4Zn_9Sb_9$ compound indicates the endothermic peak at 780 K (Figure S13) in accordance with $Na_4Zn_9Sb_9 \rightarrow$ NaZnSb + *melt* transformation at 791 K observed from *in situ* HT-PXRD. Early decomposition of $Na_4Zn_9Sb_9$ that starts above 511 K is not observed in the DSC data. Two endothermic peaks at 760 and 780 K are observed in the DSC data for $NaZn_3Sb_3$ sample. The first peak corresponds to the decomposition of $NaZn_3Sb_3$ as observed from *in situ* HT-PXRD (762 K); however, the

https://doi.org/10.1021/acs.inorgchem.1c01381
Inorg. Chem. 2021, 60, 10686−10697

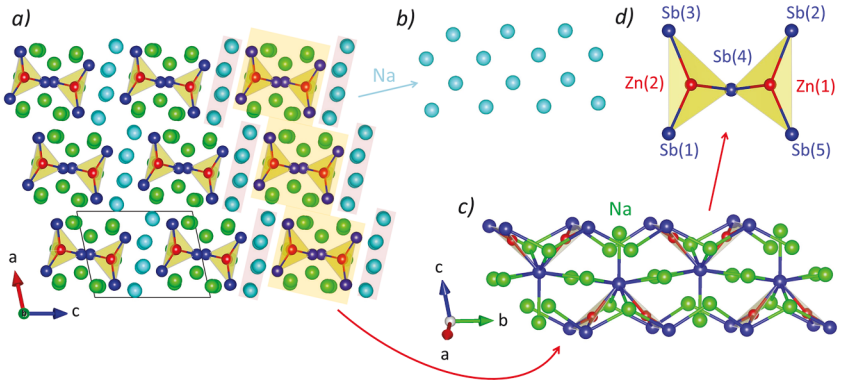

Figure 5. Crystal structure of (a) $Na_{11}Zn_2Sb_5$ (Na, green and cyan; Zn, red; Sb, blue) consisting of two building blocks: (b) Na layer as present in Na metal, (c) chains of $[Zn_2Sb_5]^{11-}$ anions bridged by Na+ cations along the *b*-direction, (d) $[Zn_2Sb_5]^{11-}$ cluster.

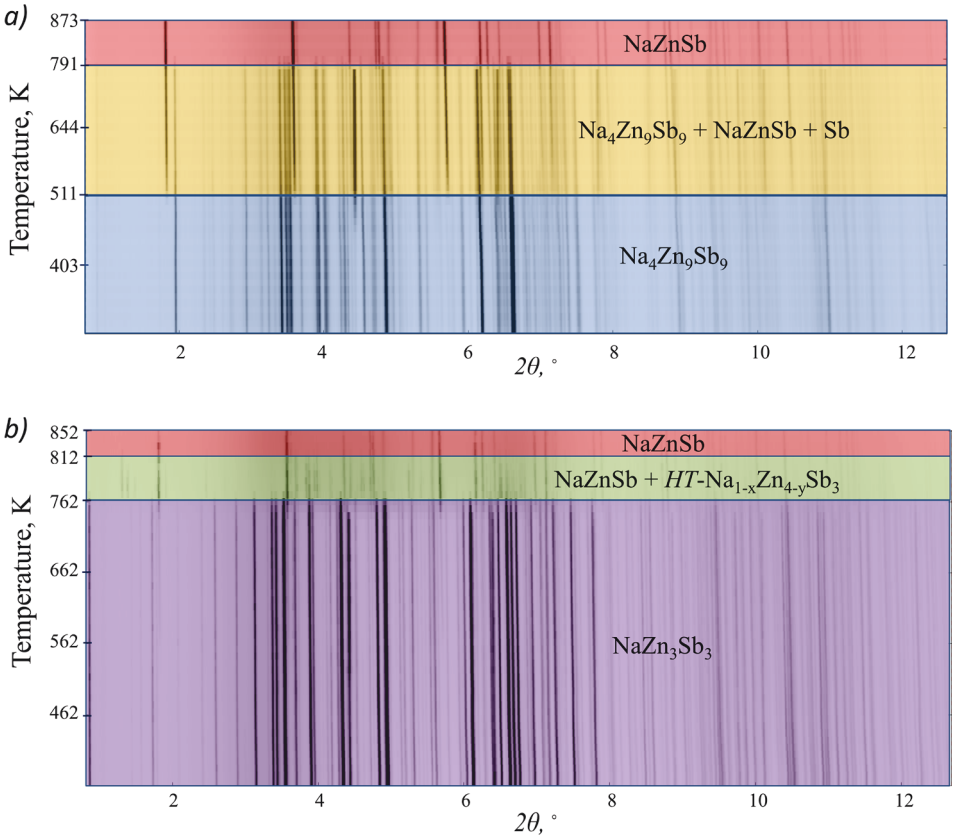

Figure 6. High-temperature *in situ* X-ray diffraction patterns, showing the transformation of powdered samples of (a) $Na_4Zn_9Sb_9$ and (b) $NaZn_3Sb_3$ sealed into evacuated silica capillary. The "waterfall" plot shows the sequence of powder XRD patterns from room temperature (bottom) to up 873 K (top). The temperature regions with distinct phase contributions are highlighted in different colors.

second peak expected at 812 K was not observed. Instead, the second endothermic peak appears at 780 K, which suggests the formation of $Na_4Zn_9Sb_9$ intermediate, which further decomposes to NaZnSb with the increasing temperature. The difference between the intermediates formed after decomposition of $NaZn_3Sb_3$ (*HT*-$Na_{1-x}Zn_{4-y}Sb_3$ according to *in situ* HT-PXRD or $Na_4Zn_9Sb_9$ from the DSC data) may originate from the drastically different geometry of the vessels (long thin capillary vs short wide crucible) and, therefore, the difference in liquid/solid phases distributions at high temperatures, variation in vapor pressure, partial Na/Zn evaporation, and side reactions with vessel material (silica), resulting in sample inhomogeneity.

The unit cell parameters and volume obtained from the Rietveld refinement of HT-PXRD data linearly increase upon heating (Figure S14). The coefficients of thermal expansion (CTE) obtained from linear fits of the data were calculated via the following equations:

$$\mathrm{CTE}\ NaZn_3Sb_3(V) = \frac{dV}{dT} \times \frac{1}{V} = 5.65(3) \times 10^{-6}K^{-1},$$

$$\mathrm{CTE}\ Na_4Zn_9Sb_9(V) = \frac{dV}{dT} \times \frac{1}{V} = 6.9(1) \times 10^{-5}K^{-1}$$

The CTEs increase in the row $NaZn_3Sb_3$–$Na_4Zn_9Sb_9$–NaZnSb (for NaZnSb: CTE (*V*) 9.58 × 10^{-5} K^{-1})[9] as the

https://doi.org/10.1021/acs.inorgchem.1c01381
Inorg. Chem. 2021, 60, 10686−10697

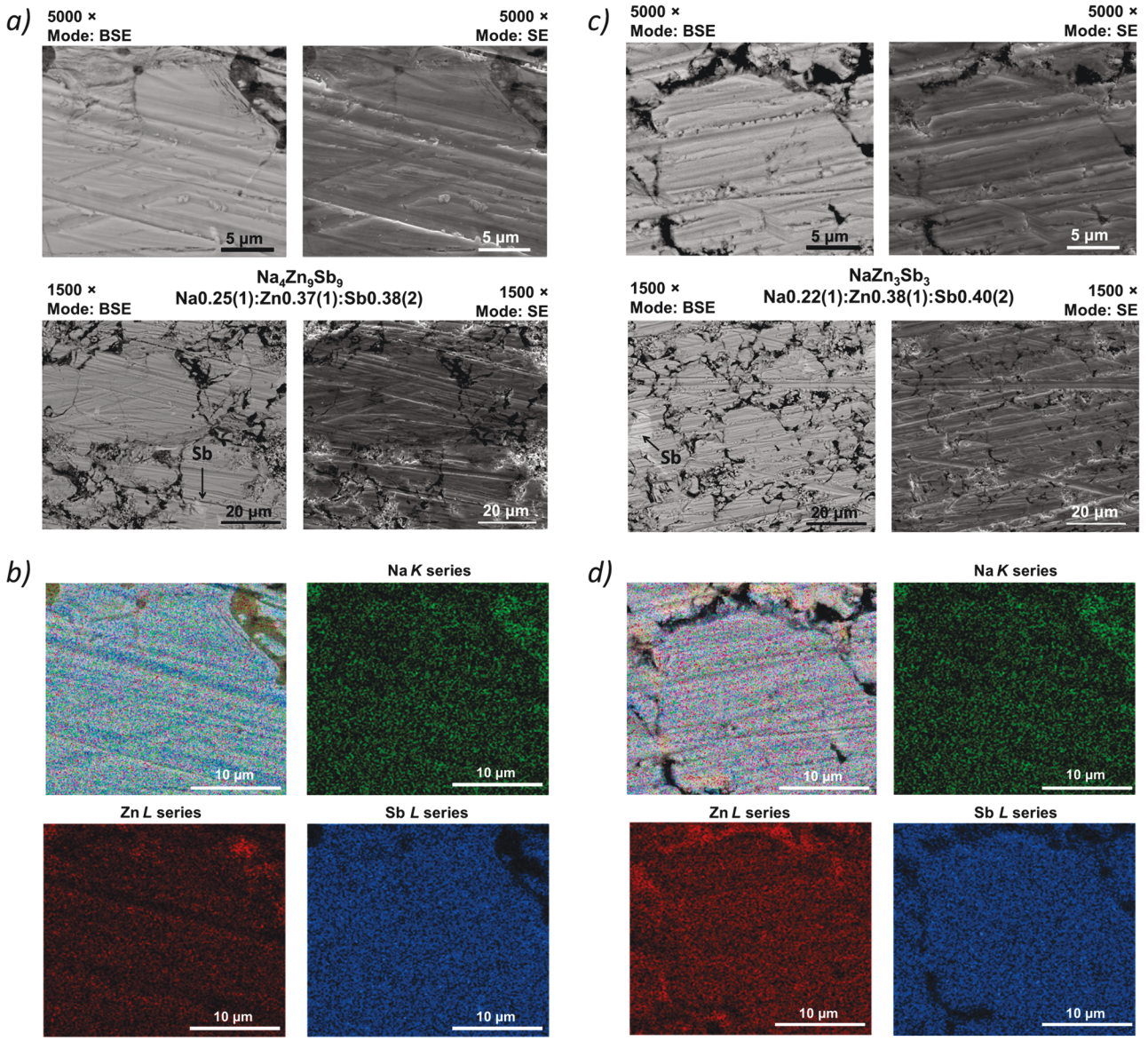

Figure 7. Scanning electron microcopy (SEM) images obtained in backscattered electrons (BSE) and secondary electrons (SE) modes and concentration maps for the samples of $Na_4Zn_9Sb_9$ (a, b) and $NaZn_3Sb_3$ (c, d) prepared via hydride route and further sintered by SPS.

structure becomes more anisotropic, *e.g.*, more pronouncedly layered (Figure 2).

Elemental Analysis of $Na_4Zn_9Sb_9$ and $NaZn_3Sb_3$. Scanning electron microscopy (SEM) images in backscattered electrons (BSE) and secondary electrons (SE) modes were collected for the polished pellets of $Na_4Zn_9Sb_9$ and $NaZn_3Sb_3$ densified by SPS (Figure 7). Compositions determined by energy-dispersive X-ray spectroscopy (EDX) analysis were averaged and normalized based on 8 different areas for each sample. The elemental distribution is homogeneous, and the average compositions are determined to be Na:Zn:Sb = 0.25(1):0.37(1):0.38(2) for $Na_4Zn_9Sb_9$ (expected ratio is 0.18:0.41:0.41) and Na:Zn:Sb = 0.22(1):0.38(1):0.40(2) for $NaZn_3Sb_3$ phase (expected ratio is 0.14:0.43:0.43), respectively. The Na content is overestimated because of the overlap between Na−K_α and Zn−L_α lines, causing difficulties in deconvoluting the Na and Zn characteristic lines in the EDX spectrum. A similar inconsistency was observed for the stoichiometric NaZnSb, with a Na:Zn:Sb ratio determined by EDX to be 1.3:1:1.[14] SEM confirmed small amounts of elemental Sb (light gray areas on the BSE-images) as the only impurity in the sintered pellets.

Low-Temperature Transport Properties of $Na_4Zn_9Sb_9$ and $NaZn_3Sb_3$. The thermoelectric properties (Figure 8) in the 10−300 K temperature range were measured for the SPS densified pellets of $Na_4Zn_9Sb_9$(compactness of 79%; 15 wt % of Sb impurity) and $NaZn_3Sb_3$ (compactness of 89%; 6 wt % of Sb impurity). Both materials exhibit positive Seebeck coefficients which gradually increase with temperature up to 19 and 32 $\mu V \cdot K^{-1}$ at 300 K for $Na_4Zn_9Sb_9$ and $NaZn_3Sb_3$ phases, respectively. This is consistent with *p*-type conductors with holes as charge carries. Both compounds show low electrical resistivity ($\sim 1 \times 10^{-4}$ Ω·m) that is only slightly temperature dependent, suggesting a bad metal behavior.

Both compounds, $Na_4Zn_9Sb_9$ (N_{cell} = 88 atoms; V_{cell} = 2176 Å^3) and $NaZn_3Sb_3$ (N_{cell} = 56 atoms; V_{cell} = 1386 Å^3) are structurally complex and show overall low thermal conductivities (~0.97−1.26 $W \cdot m^{-1} \cdot K^{-1}$ at room temperature). This can

https://doi.org/10.1021/acs.inorgchem.1c01381
Inorg. Chem. 2021, 60, 10686−10697

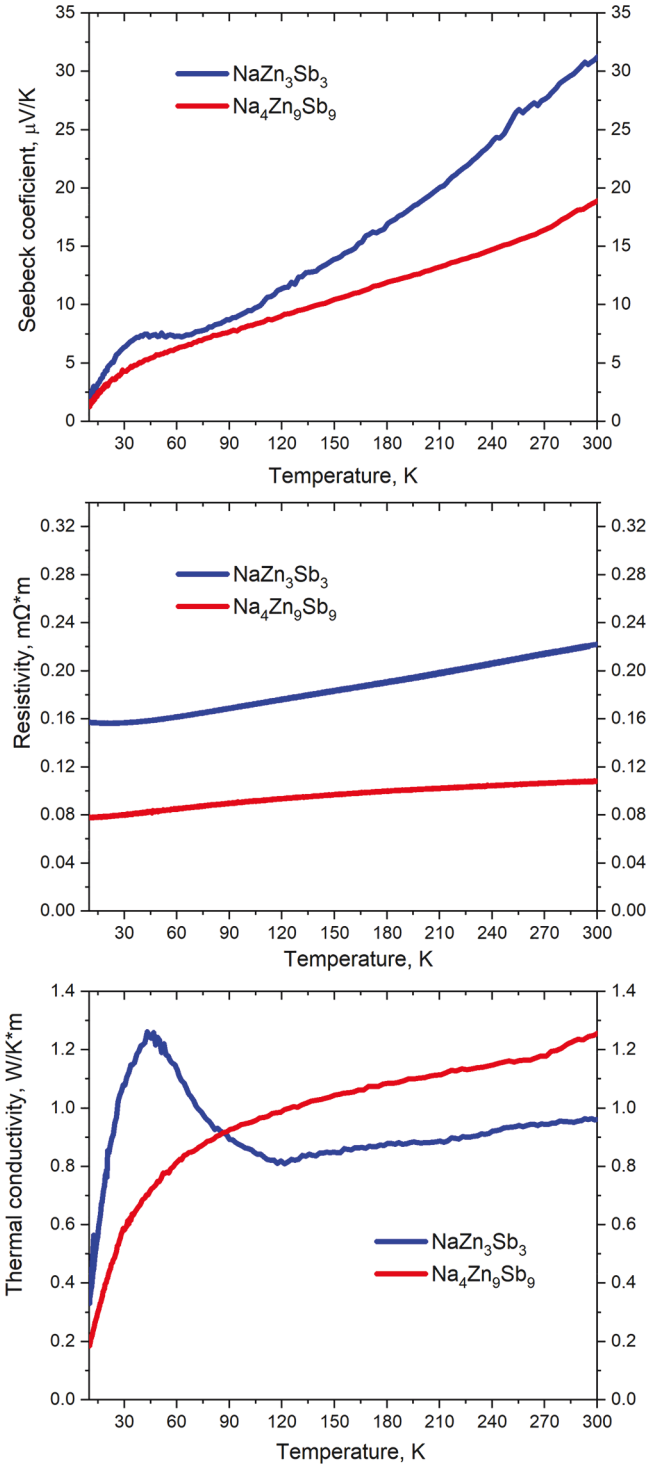

Figure 8. Temperature dependence of transport properties for $Na_4Zn_9Sb_9$ (red) and $NaZn_3Sb_3$ (blue): (top) Seebeck coefficient, (middle) electrical resistivity; (bottom) thermal conductivity (the estimated electronic thermal conductivity contribution is negligible at less than 5.4% for the $Na_4Zn_9Sb_9$ phase and less than 3.4% for the $NaZn_3Sb_3$).

be partially attributed to the disorder of Zn sites, resulting in the large ADPs for adjacent Zn and Sb atoms in the structure of $Na_4Zn_9Sb_9$, as well to the large ADPs for Zn an Sb atoms linking Na-centered polyhedra in $NaZn_3Sb_3$. The thermal conductivity of $NaZn_3Sb_3$ increases with increasing temperature from 0.35 $W{\cdot}m^{-1}{\cdot}K^{-1}$ at 10 K to 0.97 $W{\cdot}m^{-1}{\cdot}K^{-1}$ at 300 K with a maximum at ~45 K. On the contrary, the $Na_4Zn_9Sb_9$ compound lacks such a peak at low temperature. A peak in thermal conductivity in the range of 50−150 K is typical for crystalline solids,[62] while it is absent for glass materials due to the lack of grain boundary scattering at low temperatures. In addition, low, glass-like thermal conductivities of crystalline Ge and Sn clathrates is attributed to enormous displacements ("rattling") of the guest cations inside oversized polyhedral cages.[63−66] The lack of the peak in thermal conductivity for $Na_4Zn_9Sb_9$ can be attributed to the disorder in Zn sites, similar to the case of Zn_4Sb_3.[31] In both $Na_4Zn_9Sb_9$ and $NaZn_3Sb_3$ structures, Na^+ cations occupy Zn−Sb polyhedra and have large anisotropic displacement parameters, contributing to the overall low thermal conductivity. The low thermal conductivity could be partially attributed to the moderate pellet densities (79% and 89%). The total thermal conductivity (κ_{total}) consists of electronic thermal conductivity, κ_e, and the lattice thermal conductivity, κ_L: $\kappa_{total} = \kappa_e + \kappa_L = LT/\rho + \kappa_L$, where L is the Lorenz number and ρ is resistivity. For metals with high concentrations of charge carriers, the Lorenz number approaches the Sommerfeld limit, $L = 2.45 \times 10^{-8} W{\cdot}\Omega{\cdot}K^{-2}$ (free electron model). The L estimated using experimental Seebeck coefficients[67] results in similar values of L, within the $2.27-2.48 \times 10^{-8} W{\cdot}\Omega{\cdot}K^{-2}$ range for $Na_4Zn_9Sb_9$ and $NaZn_3Sb_3$ phases in 300−10 K temperature range. Thus, the conservative value of $L = 2.45 \times 10^{-8}$ $W{\cdot}\Omega{\cdot}K^{-2}$ was used. The estimated electronic thermal conductivity is 5.4% and 3.4% of total thermal conductivity for $Na_4Zn_9Sb_9$ and $NaZn_3Sb_3$ phases, respectively.

The thermoelectric figure-of-merit $zT = \alpha^2 \times T/(\kappa \times \rho)$ (ρ, resistivity; κ, thermal conductivity; α, Seebeck coefficient; T, temperature) amounts to $\sim 1.0 \times 10^{-3}$ for $Na_4Zn_9Sb_9$ and to $\sim 1.3 \times 10^{-3}$ for $NaZn_3Sb_3$ at room temperature. The low zT for both compounds can be attributed to low Seebeck coefficient. The related alkali, alkaline-earth zinc antimonides $CaZn_2Sb_2$, $SrZn_2Sb_2$, NaZnSb[14,36] or even state-of-the-art $Yb_{14}MnSb_{11}$[68] also have low values of zT at room temperature (up to 0.05−0.1) but with the increasing of temperature, the figure of merit increases considerably. Since $Na_4Zn_9Sb_9$ and $NaZn_3Sb_3$ are stable upon heating until 500−700 K, high temperature measurements of thermoelectric properties of these materials may lead to higher zT.

Theoretical Calculations. Electronic band structures and total and partial densities of states (DOS) for $NaZn_3Sb_3$, $Na_4Zn_9Sb_9$, and $Na_{11}Zn_2Sb_5$ compounds are shown in Figure 9. An ideal structural model for $Na_4Zn_9Sb_9$ without atomic sites splitting was used for calculations. While $Na_{11}Zn_2Sb_5$ and $NaZn_3Sb_3$ are electron balanced, analysis of the structure of $Na_4Zn_9Sb_9$ indicates a 1 electron deficiency. $Na_{11}Zn_2Sb_5$ was predicted to be a semiconductor with a direct band gap of ~0.7 eV. Due to the high chemical reactivity of the compound, the experimental measurement of the band gap was not performed. $NaZn_3Sb_3$ and $Na_4Zn_9Sb_9$ compounds were found to be metallic, with a nonzero density of states at the Fermi level consistent with the electronic transport property measurements. For all three compounds, Sb and Zn atomic orbitals have major contributions to the DOS. This is in accordance with Na donating its electron to the [Zn−Sb] covalent framework. In the case of $NaZn_3Sb_3$, the Fermi level resides in a pseudogap with DOS(E_F) ~ 1.5 states eV^{-1}/atom, while in $Na_4Zn_9Sb_9$, the pseudogap is shifted to ~0.4 eV above the Fermi level. The integration of DOS reveals that $Na_4Zn_9Sb_9$ composition is one electron short of Fermi level to fall into

https://doi.org/10.1021/acs.inorgchem.1c01381
Inorg. Chem. 2021, 60, 10686−10697

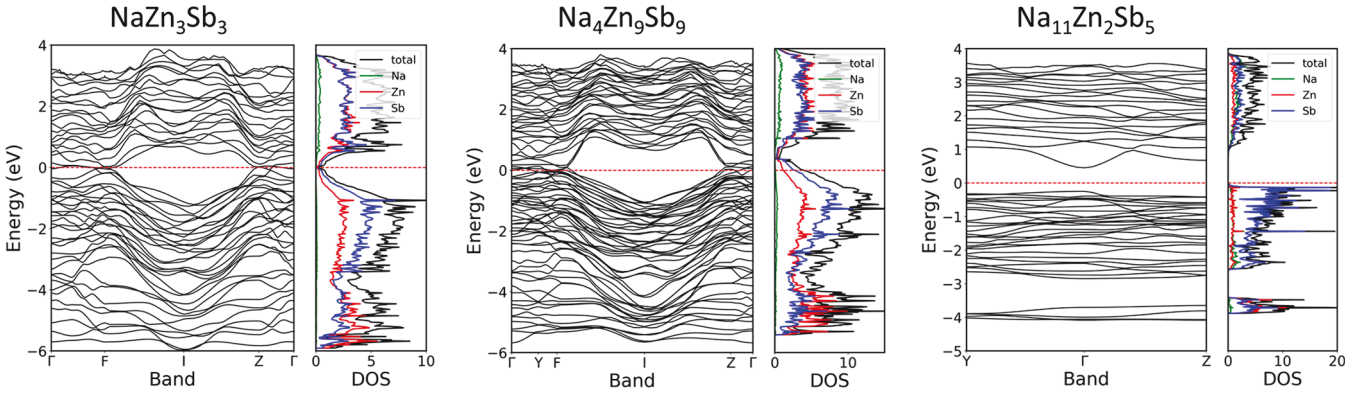

Figure 9. Band structures with total and partial DOS representations for $NaZn_3Sb_3$, $Na_4Zn_9Sb_9$, and $Na_{11}Zn_2Sb_5$. The zero energy is taken at the Fermi level E_F. The atomic contributions of Na (green), Zn (red), and Sb (blue) are shown.

pseudogap (Figure S15). This is in agreement with the 1 electron deficiency obtained via electron counting by considering Na and Zn as +1 and +2 cations, respectively, and anionic Sb with either −3 or −2 oxidation state depending on the number of Sb−Sb covalent bonds (*vide supra*, Table S12).

Taking into account the low measured thermal conductivity and low electrical resistivity of $NaZn_3Sb_3$ and $Na_4Zn_9Sb_9$ compounds, chemical substitution of the pnictogen site (*e.g.*, Sb^{3-} with the more electronegative As^{3-} or Te^{2-}) may promote further band separation and increase the Seebeck coefficient,[69] while simultaneous aliovalent (*p*-type) doping of the Zn site (*e.g.*, Zn^{2+}/Cu^{+}) might lead to a high carrier concentration, enhancing the $zT = \alpha^2 \times T/(\kappa \times \rho)$.

CONCLUSIONS

By using high-temperature *in situ* powder X-ray diffraction and a hydride synthesis method, a compositional space in the Na−Zn−Sb system was screened, resulting in the discovery of three new sodium zinc antimonides: $Na_{11}Zn_2Sb_5$, $Na_4Zn_9Sb_9$, and $NaZn_3Sb_3$. The crystal structures of the latter two compounds belong to new structure types and feature complex frameworks of edge-shared and vertex-shared $Zn@Sb_4$ tetrahedra hosting Na^+ cation within their channels. The structure of $Na_{11}Zn_2Sb_5$ has polyanionic $[Zn_2Sb_5]^{11-}$ clusters with unusual 3-coordinated Zn atoms. The composition of $Na_{11}Zn_2Sb_5$ belongs to a group of electron-balanced phases (Na_3Sb−Zn_3Sb_2), while $Na_4Zn_9Sb_9$ and $NaZn_3Sb_3$ are electron-deficient, considering the oxidation states for Na^+, Zn^{2+}, and Sb^{3-}. Analysis of the structures of $NaZn_3Sb_3$ and $Na_4Zn_9Sb_9$ revealed covalent bonds between some of the Sb atoms, which results in formally electron-balanced $NaZn_3Sb_3$; yet, there is 1 electron deficiency in $Na_4Zn_9Sb_9$. The tendency for an electron deficiency is in agreement with the determined positive Seebeck coefficient of the $Na_4Zn_9Sb_9$ and $NaZn_3Sb_3$ compounds indicating *p*-type conductivity. The compounds are structurally complex and exhibit low thermal conductivities (~0.97−1.26 $W \cdot m^{-1} \cdot K^{-1}$ at room temperature). *In situ* synchrotron powder X-ray diffraction studies show the complete decomposition of $Na_4Zn_9Sb_9$ and $NaZn_3Sb_3$ into NaZnSb above ~800 K, making conventional high temperature solid state synthesis unsuitable for their preparation. Advantages of the hydride route (highly reactive precursors ball-milled in the desired ratios) allow for the lowering of the reaction temperature making $Na_4Zn_9Sb_9$ and $NaZn_3Sb_3$ compounds accessible. The metal hydride synthetic method has proven, yet again, to be a highly effective tool in both the discovery and synthesis of hard-to-obtain phases.

ASSOCIATED CONTENT

Supporting Information

The Supporting Information is available free of charge at https://pubs.acs.org/doi/10.1021/acs.inorgchem.1c01381.

Interatomic distances, Rietveld refinement plots and tables with parameters of XRD data collection and refinement (PDF)

Accession Codes

CCDC 2035042 2035044 and 2063968−2063969 contain the supplementary crystallographic data for this paper. These data can be obtained free of charge via www.ccdc.cam.ac.uk/data_request/cif, or by emailing data_request@ccdc.cam.ac.uk, or by contacting The Cambridge Crystallographic Data Centre, 12 Union Road, Cambridge CB2 1EZ, UK; fax: +44 1223 336033.

AUTHOR INFORMATION

Corresponding Author

Julia V. Zaikina − *Department of Chemistry, Iowa State University, Ames, Iowa 50011, United States;* orcid.org/0000-0002-8755-1926; Email: yzaikina@iastate.edu

Authors

Volodymyr Gvozdetskyi − *Department of Chemistry, Iowa State University, Ames, Iowa 50011, United States*

Shannon J. Lee − *Department of Chemistry, Iowa State University, Ames, Iowa 50011, United States; Ames Laboratory, U.S. Department of Energy, Ames, Iowa 50011, United States;* orcid.org/0000-0002-7541-3286

Bryan Owens-Baird − *Department of Chemistry, Iowa State University, Ames, Iowa 50011, United States; Ames Laboratory, U.S. Department of Energy, Ames, Iowa 50011, United States;* orcid.org/0000-0003-3128-5363

Juli-Anna Dolyniuk − *Department of Chemistry, University of California at Davis, Davis, California 95616, United States*

Tori Cox − *Department of Chemistry, Iowa State University, Ames, Iowa 50011, United States*

Renhai Wang − *Department of Physics, University of Science and Technology of China, Hefei 230026, China*

Zijing Lin − *Department of Physics, University of Science and Technology of China, Hefei 230026, China;* orcid.org/0000-0001-9270-1717

Kai-Ming Ho − *Department of Physics, University of Science and Technology of China, Hefei 230026, China; Department of Physics and Astronomy, Iowa State University, Ames, Iowa 50011, United States*

Complete contact information is available at: https://pubs.acs.org/10.1021/acs.inorgchem.1c01381

Notes

The authors declare no competing financial interest.

■ ACKNOWLEDGMENTS

We thank Dr. Warren Straszheim (Materials Analysis Research Laboratory, Iowa State University) for help with SEM/EDX. Dr. Wenqian Xu and Dr. Andrey Yakovenko at the 17-BM beamline, APS ANL, for help with high-temperature synchrotron powder XRD data collection. Financial support from the National Science Foundation (DMR-1944551) NSF CAREER award is gratefully acknowledged. The work at Ames Laboratory was supported by the U.S. Department of Energy (DOE), Office of Science, Basic Energy Sciences, Materials Science and Engineering Division, under Contract No. DE-AC02-07CH11358, including a grant of computer time at the National Energy Research Scientific Computing Center (NERSC) in Berkeley, CA. Work at University of Science and Technology of China was supported by the National Natural Science Foundation of China (11774324 & 12074362) and the Supercomputing Center of USTC. Use of the Advanced Photon Source at Argonne National Laboratory was supported by the U.S. Department of Energy, Office of Science, Office of Basic Energy Sciences, under Contract No. DE-AC02-06CH11357.

■ REFERENCES

(1) Schhmidt, M.; Schhmidt, J.; Grin, Yu; Bohm, A.; Kieback, B.; Scholl, R.; Schubert, T.; Weissgarber, T.; Zumdick, K. Production of magnesium silicide compounds useful for making low-density building materials comprises reacting magnesium hydride with silicon. Patent #WO02083561 2002.

(2) Schmidt, J.; Grin, Yu.; Production of high-purity magnesium boride compounds useful for superconductor manufacture comprises reacting magnesium hydride with boron Patent #DE10117877 2002.

(3) Schmidt, J.; Schnelle, W.; Grin, Yu; Kniep, R. Pulse plasma synthesis and chemical bonding in magnesium diboride. *Solid State Sci.* **2003**, *5*, 535−539.

(4) Schmidt, J.; Niewa, R.; Schmidt, M.; Grin, Yu Spark Plasma Sintering Effect on the Decomposition of MgH_2. *J. Am. Ceram. Soc.* **2005**, *88*, 1870−1874.

(5) Reinfried, N.; Schmidt, J.; Kieback, B.; Grin, Yu Spark plasma preparation of Mg_2Si and Mg_2Si-Mg composite. *Proceedings PM2004 Powder Metallurgy World Congress, Wien* **2004**, 247.

(6) Ma, X.; Xu, F.; Atkins, T. M.; Goforth, A. M.; Neiner, D.; Navrotsky, A.; Kauzlarich, S. M. A versatile low temperature synthetic route to Zintl phase precursors: Na_4Si_4, Na_4Ge_4 and K_4Ge_4 as examples. *Dalton Trans.* **2009**, *0*, 10250−10255.

(7) Yi, T.; Chen, S.; Li, S.; Yang, H.; Bux, S.; Bian, Z.; Katcho, N. A.; Shakouri, A.; Mingo, N.; Fleurial, J. P.; Browning, N. D.; Kauzlarich, S. M. Synthesis and characterization of Mg_2Si/Si nanocomposites prepared from MgH_2 and silicon, and their thermoelectric properties. *J. Mater. Chem.* **2012**, *22*, 24805−24813.

(8) Zaikina, J. V.; Batuk, M.; Abakumov, A. M.; Navrotsky, A.; Kauzlarich, S. M. Facile Synthesis of $Ba_{1-x}K_xFe_2As_2$ Superconductors via Hydride Route. *J. Am. Chem. Soc.* **2014**, *136*, 16932−16939.

(9) Zaikina, J. V.; Kwong, M. Y.; Baccam, B.; Kauzlarich, S. M. Superconductor-in-an-hour: Spark Plasma synthesis of Co and Ni-doped $BaFe_2As_2$. *Chem. Mater.* **2018**, *30*, 8883−8890.

(10) Cox, T.; Gvozdetskyi, V.; Owens-Baird, B.; Zaikina, J. V. Rapid phase screening via hydride route: a discovery of $K_{8-x}Zn_{18+3x}Sb_{16}$. *Chem. Mater.* **2018**, *30*, 8707−8715.

(11) Gvozdetskyi, V.; Hanrahan, M. P.; Ribeiro, R. A.; Kim, T.; Zhou, L.; Rossini, A. J.; Canfield, P. C.; Zaikina, J. V. Hydride route to alkali metal borides: a case study of lithium nickel borides. *Chem. - Eur. J.* **2019**, *25*, 4123−4135.

(12) Gvozdetskyi, V.; Bhaskar, G.; Batuk, M.; Zhao, X.; Wang, R.; Carnahan, S. L.; Hanrahan, M. P.; Ribeiro, R. A.; Canfield, P. C.; Rossini, A. J.; Wang, C. Z.; Ho, K.-M.; Hadermann, J.; Zaikina, J. V. Computationally-driven discovery of a family of layered LiNiB polymorphs. *Angew. Chem., Int. Ed.* **2019**, *58*, 15855−15862.

(13) Perez, C. J.; Bates, V. J.; Kauzlarich, S. M. Hydride Synthesis and Thermoelectric Properties of Type-I Clathrate $K_8E_8Ge_{38}$ (E = Al, Ga, In). *Inorg. Chem.* **2019**, *58*, 1442−1450.

(14) Gvozdetskyi, V.; Owens-Baird, B.; Hong, S.; Zaikina, J. V. Thermal stability and thermoelectric properties of NaZnSb. *Materials* **2019**, *12*, 48−62.

(15) Gvozdetskyi, V.; Owens-Baird, B.; Hong, S.; Cox, T.; Bhaskar, G.; Harmer, C.; Sun, Y.; Zhang, F.; Wang, C. Z.; Ho, K. M.; Zaikina, J. V. From $NaZn_4Sb_3$ to *HT*-$Na_{1-x}Zn_{4-y}Sb_3$: panoramic hydride synthesis, structural diversity, and thermoelectric properties. *Chem. Mater.* **2019**, *31*, 8695−8707.

(16) Cox, T.; Gvozdetskyi, V.; Bertolami, M.; Lee, S.; Shipley, K.; Lebedev, O. I.; Zaikina, J. V. Clathrate XI $K_{58}Zn_{122}Sb207$: A new branch on the clathrate family tree. *Angew. Chem., Int. Ed.* **2021**, *60*, 415−423.

(17) Gvozdetskyi, V.; Sun, Y.; Zhao, X.; Bhaskar, G.; Carnahan, S. L.; Harmer, C. P.; Zhang, F.; Ribeiro, R. A.; Canfield, P. C.; Rossini, A. J.; Wang, C.-Z.; Ho, K.-M.; Zaikina, J. V. Lithium Nickel Borides: evolution of [NiB] layers driven by Li pressure. *Inorg. Chem. Front.* **2021**, *8*, 1675−1685.

(18) Justl, A. P.; Cerretti, G.; Bux, S. K.; Kauzlarich, S. M. Hydride assisted synthesis of the high temperature thermoelectric phase: $Yb_{14}MgSb_{11}$. *J. Appl. Phys.* **2019**, *126*, 165106.

(19) *ICSD − the Inorganic Crystal Structure Database*; FIZ − Karlsruhe, 2021.

(20) Schroeder, G.; Schuster, H. U. LiZnSb, an additional ternary phase with a Wurzit-type lattice (*in German*). *Z. Naturforsch., B: J. Chem. Sci.* **1975**, *30*, 978−979.

(21) White, M. A.; Miller, G. J.; Vela, J. Polytypism and unique site preference in LiZnSb: a superior thermoelectric reveals its true colors. *J. Am. Chem. Soc.* **2016**, *138*, 14574−14577.

(22) Schroeder, G.; Schuster, H. U. Röntgenographische Untersuchungen im System Lithium-Zink-Antimon. *Z. Anorg. Allg. Chem.* **1977**, *431*, 217−220.

(23) Savelsberg, G.; Schaefer, H. On Ternary Pnictides and Chalkogenides of Alkaline Metals and IB-resp. II B-Elements (*in German*). *Z. Naturforsch., B: J. Chem. Sci.* **1978**, *33*, 370−373.

(24) He, H.; Stoyko, S. S.; Mar, A.; Bobev, S. Ternary $K_2Zn_5As_4$-type pnictides $Rb_2Cd_5As_4$ and $Rb_2Zn_5Sb_4$, and the solid solution $Rb_2Cd_5(As,Sb)_4$. *Acta Crystallogr., Sect. C: Cryst. Struct. Commun.* **2013**, *69*, 455−459.

(25) Owens-Baird, B.; Wang, L.-L.; Lee, S.; Kovnir, K. Synthesis, crystal and electronic structure of layered *AM*Sb compounds (A = Rb, Cs; M = Zn, Cd). *Z. Anorg. Allg. Chem.* **2020**, *646*, 1079.

(26) Liu, Y.; Wu, L.-M.; Li, L.-H.; Du, S. W.; Corbett, J. D.; Chen, L. The antimony-based type I Clathrate Compounds $Cs_8Cd_{18}Sb_{28}$ and $Cs_8Zn_{18}Sb_{28}$. *Angew. Chem., Int. Ed.* **2009**, *48*, 5305−5308.

(27) Pothin, R.; Ayral, R. M.; Berche, A.; Granier, D.; Rouessac, F.; Jund, P. Preparation and properties of ZnSb thermoelectric material through mechanical-alloying and Spark Plasma Sintering. *Chem. Eng. J.* **2016**, *299*, 126−134.

(28) Lo, C. T.; Ortiz, B. R.; Toberer, E.; He, A.; Svitlyk, V.; Chernyshov, D.; Kolodiazhny, T.; Lidin, S.; Mozharivskyj, Y. Synthesis, Structure, and Thermoelectric Properties of α-Zn_3Sb_2 and Comparison to β-$Zn_{13}Sb_{10}$. *Chem. Mater.* **2017**, *29*, 5249−5258.

(29) Wang, J.; Kovnir, K. Elusive β-Zn_8Sb_7: A New Zinc Antimonide Thermoelectric. *J. Am. Chem. Soc.* **2015**, *137*, 12474−12477.

(30) Caillat, T.; Fleurial, J.-P.; Borshchevsky, A. Preparation and thermoelectric properties of semiconducting Zn_4Sb_3. *J. Phys. Chem. Solids* **1997**, *58*, 1119−1125.
(31) Snyder, G. J.; Christensen, M.; Nishibori, E.; Caillat, T.; Iversen, B. B. Disordered zinc in Zn_4Sb_3 with phonon-glass and electron-crystal thermoelectric properties. *Nat. Mater.* **2004**, *3*, 458−463.
(32) Tang, D.; Zhao, W.; Yu, J.; Wei, P.; Zhou, H.; Zhu, W.; Zhang, Q. Crystal structure, chemical bond and enhanced performance of β-Zn_4Sb_3 compounds with interstitial indium dopant. *J. Alloys Compd.* **2014**, *601*, 50−56.
(33) Zhang, H.; Zhao, J.-T.; Grin, Yu; Wang, X.-J.; Tang, M.-B.; Man, Z.-Y.; Chen, H.-H.; Yang, X.-X. A new type of thermoelectric material, $EuZn_2Sb_2$. *J. Chem. Phys.* **2008**, *129*, 164713.
(34) Wang, X.-J.; Tang, M.-B.; Chen, H.-H.; Yang, X.-X.; Zhao, J.-T.; Burkhard, U. Synthesis and high thermoelectric efficiency of Zintl phase $YbCd_{2-x}Zn_xSb_2$. *Appl. Phys. Lett.* **2009**, *94*, 092106.
(35) Zhang, H.; Fang, L.; Tang, M.-B.; Chen, H.-H.; Yang, X.-X.; Guo, X.; Zhao, J.-T.; Grin, Yu Synthesis and properties of $CaCd_2Sb_2$ and $EuCd_2Sb_2$. *Intermetallics* **2010**, *18*, 193−198.
(36) Toberer, E. S.; May, A. F.; Melot, B. C.; Flage-Larsend, E.; Snyder, G. J. Electronic structure and transport in thermoelectric compounds AZn_2Sb_2 (A = Sr, Ca, Yb, Eu). *Dalton Trans.* **2010**, *39*, 1046−1054.
(37) Gascoin, F.; Ottensmann, S.; Stark, D.; Haile, S. M.; Snyder, G. J. Zintl phases as thermoelectric materials: Tuned transport properties of the compounds $Ca_xYb_{1-x}Zn_2Sb_2$. *Adv. Funct. Mater.* **2005**, *15*, 1860−1864.
(38) Chen, C.; Xue, W.; Li, S.; Zhang, Z.; Li, X.; Wang, X.; Liu, Y.; Sui, J.; Liu, X.; Cao, F.; Ren, Z.; Chu, C.-W.; Wang, Y.; Zhang, Q. Zintl-phase Eu_2ZnSb_2: A promising thermoelectric material with ultralow thermal conductivity. *Proc. Natl. Acad. Sci. U. S. A.* **2019**, *116*, 2831−2836.
(39) Chen, C.; Xue, W.; Li, X.; Lan, Y.; Zhang, Z.; Wang, X.; Zhang, F.; Yao, H.; Li, S.; Sui, J.; Han, P.; Liu, X.; Cao, F.; Wang, Y.; Zhang, Q. Enhanced Thermoelectric Performance of Zintl Phase $Ca_9Zn_{4+x}Sb_9$ by beneficial disorder on the selective cationic site. *ACS Appl. Mater. Interfaces* **2019**, *11*, 37741−37747.
(40) Ovchinnikov, A.; Bobev, S. Zintl phases with group 15 elements and the transition metals: A brief overview of pnictides with diverse and complex structures. *J. Solid State Chem.* **2019**, *270*, 346−359.
(41) Kauzlarich, S. M.; Zevalkink, A.; Toberer, E.; Snyder, G. J. Zintl Phases: Recent Developments in Thermoelectrics and Future Outlook. In *Thermoelectric materials and devices*. Nandhakumar, I.; White, M. M.; Beeby, S., Eds.; Book Series: RSC Energy and Environment Series. 2017, *17*, 1−26.
(42) Snyder, G. J.; Toberer, E. S. Complex thermoelectric materials. *Nat. Mater.* **2008**, *7*, 105−114.
(43) Haynes, A. S.; Stoumpos, C. C.; Chen, H.; Chica, D.; Kanatzidis, M. G. Panoramic Synthesis as an Effective Materials Discovery Tool: The System Cs/Sn/P/Se as a Test Case. *J. Am. Chem. Soc.* **2017**, *139*, 10814−10821.
(44) Kanatzidis, M. G. Discovery-Synthesis, Design, and Prediction of Chalcogenide Phases. *Inorg. Chem.* **2017**, *56*, 3158−3173.
(45) Vasquez, G.; Huq, A.; Latturner, S. E. In Situ Neutron Diffraction Studies of the Metal Flux Growth of Ba/Yb/Mg/Si Intermetallics. *Inorg. Chem.* **2019**, *58*, 8111−8119.
(46) Woo, K. E.; Wang, J.; Mark, J.; Kovnir, K. Directing boron-phosphorus bonds in crystalline solid: oxidative polymerization of P = B=P monomers into 1D chains. *J. Am. Chem. Soc.* **2019**, *141*, 13017−13021.
(47) *PDXL: Integrated X-ray powder diffraction software*, Version 2.8.1.1. Rigaku, 2018.
(48) *Apex3*, Version 2017.3, Bruker, USA.
(49) Sheldrick, G. M. A short history of SHELX. *Acta Crystallogr., Sect. A: Found. Crystallogr.* **2008**, *A64*, 112−122.
(50) Spek, A. L. Structure validation in chemical crystallography. *Acta Crystallogr., Sect. D: Biol. Crystallogr.* **2009**, *D65*, 148−155.
(51) Toby, B. H.; Von Dreele, R. B. GSAS-II: the genesis of a modern open-source all purpose crystallography software package. *J. Appl. Crystallogr.* **2013**, *46*, 544−549.
(52) Chupas, P. J.; Chapman, K. W.; Kurtz, C.; Hanson, J. C.; Lee, P. L.; Grey, C. P. A versatile sample-environment cell for non-ambient X-ray scattering experiments. *J. Appl. Crystallogr.* **2008**, *41*, 822−824.
(53) Kresse, G.; Furthmuller, J. Efficiency of ab-initio total energy calculations for metals and semiconductors using a plane-wave basis set. *Comput. Mater. Sci.* **1996**, *6*, 15−50.
(54) Kresse, G.; Furthmuller, J. Efficient iterative schemes for ab initio total-energy calculations using a plane-wave basis set. *Phys. Rev. B: Condens. Matter Mater. Phys.* **1996**, *54*, 11169−11186.
(55) Kresse, G.; Joubert, D. From ultrasoft pseudopotentials to the projector augmented-wave method. *Phys. Rev. B: Condens. Matter Mater. Phys.* **1999**, *59*, 1758−1775.
(56) Bloechl, P. E. Projector augmented-wave method. *Phys. Rev. B: Condens. Matter Mater. Phys.* **1994**, *50*, 17953−17979.
(57) Perdew, J. P.; Burke, K.; Ernzerhof, M. Generalized Gradient Approximation Made Simple. *Phys. Rev. Lett.* **1996**, *77*, 3865−3868.
(58) Carter, F. L.; Mazelsky, R. The ZnSb structure; A further enquiry. *J. Phys. Chem. Solids* **1964**, *25*, 571−581.
(59) Karttunen, A. J.; Fässler, T. F.; Linnolahti, M.; Pakkanen, T. A. Structural principles of semiconducting Group 14 clathrate frameworks. *Inorg. Chem.* **2011**, *50* (5), 1733−1742.
(60) Saparov, B.; Bobev, S.; Ozbay, A.; Nowak, E. R. Synthesis, structure and physical properties of the new Zintl phases $Eu_{11}Zn_6Sb_{12}$ and $Eu_{11}Cd_6Sb_{12}$. *J. Solid State Chem.* **2008**, *181* (10), 2690−2696.
(61) Wang, Y.; Qin, Q.; Sanga, R.; Xu, L. $K_{11}Cd_2Sb_5$ built of an unprecedented planar $CdSb_3$ triangle. *Dalton Trans.* **2015**, *44*, 18316−18319.
(62) Beekman, M.; Cahill, D. G. Inorganic crystals with glass-like and ultralow thermal conductivities. *Cryst. Res. Technol.* **2017**, *52*, 1700114.
(63) Wang, J.; Wang, L. L.; Kovnir, K. Phonon glass behavior beyond traditional cage structures: synthesis, crystal and electronic structure, and properties of KMg_4Sb_3. *J. Mater. Chem. A* **2018**, *6*, 4759−4767.
(64) Cohn, L.; Nolas, G. S.; Fessatidis, V.; Metcalf, T. H.; Slack, G. A. Glasslike heat conduction in high-mobility crystalline semiconductors. *Phys. Rev. Lett.* **1999**, *82*, 779−782.
(65) Sales, B. C.; Chakoumakos, B. C.; Jin, R.; Thompson, J. R.; Mandrus, D. Structural, magnetic, thermal, and transport properties of $X_8Ga_{16}Ge_{30}$ (X = Eu, Sr, Ba) single crystals. *Phys. Rev. B: Condens. Matter Mater. Phys.* **2001**, *63*, 245113.
(66) Christensen, S.; Schmøkel, M. S.; Borup, K. A.; Madsen, G. K. H.; McIntyre, G. J.; Capelli, S. C.; Christensen, M.; Iversen, B. B. Glass-like" thermal conductivity gradually induced in thermoelectric $Sr_8Ga_{16}Ge_{30}$ clathrate by off-centered guest atoms. *J. Appl. Phys.* **2016**, *119*, 18.
(67) Kim, H. S.; Gibbs, Z. M.; Tang, Y.; Wang, H.; Snyder, G. J. Characterization of Lorenz number with Seebeck coefficient measurement. *APL Mater.* **2015**, *3*, 041506−041511.
(68) Brown, S. R.; Kauzlarich, S. M.; Gascoin, F.; Snyder, G. J. $Yb_{14}MnSb_{11}$: new high efficiency thermoelectric material for power generation. *Chem. Mater.* **2006**, *18*, 1873−1877.
(69) Zeier, W. G.; Zevalkink, A.; Gibbs, Z. M.; Hautier, G.; Kanatzidis, M. G.; Snyder, G. J. Thinking like a chemist: intuition in thermoelectric materials. *Angew. Chem., Int. Ed.* **2016**, *55*, 6826−6841.

https://doi.org/10.1021/acs.inorgchem.1c01381
Inorg. Chem. 2021, 60, 10686−10697